

Shear wave dispersion behaviors of soft, vascularized tissues from the microchannel flow model

K J Parker¹, J Ormachea¹, S A McAleavey², R W Wood³,
J J Carroll-Nellenback⁴ and R K Miller³

¹ Department of Electrical and Computer Engineering, University of Rochester, Hopeman Building, Box 270126, Rochester, NY 14627, USA

² Department of Biomedical Engineering, University of Rochester, Goergen Building, Box 270168, Rochester, NY 14627, USA

³ Department of Obstetrics and Gynecology, University of Rochester Medical Center, 601 Elmwood Ave., Box 668, Rochester, NY 14642, USA

⁴ Center for Integrated Research Computing, University of Rochester, Taylor Hall, Box 270197, Rochester, NY 14627, USA

E-mail: kevin.parker@rochester.edu

Received 19 November 2015, revised 12 April 2016

Accepted for publication 25 April 2016

Published 9 June 2016



CrossMark

Abstract

The frequency dependent behavior of tissue stiffness and the dispersion of shear waves in tissue can be measured in a number of ways, using integrated imaging systems. The microchannel flow model, which considers the effects of fluid flow in the branching vasculature and microchannels of soft tissues, makes specific predictions about the nature of dispersion. In this paper we introduce a more general form of the 4 parameter equation for stress relaxation based on the microchannel flow model, and then derive the general frequency domain equation for the complex modulus. Dispersion measurements in liver (*ex vivo*) and whole perfused placenta (post-delivery) correspond to the predictions from theory, guided by independent stress relaxation measurements and consideration of the vascular tree structure.

Keywords: shear waves, elastography, dispersion, rheological models, tissue characterization

(Some figures may appear in colour only in the online journal)

1. Introduction

The proliferation of technologies for estimating and imaging the biomechanical properties of tissues (Parker *et al* 2011) has renewed interest in appropriate rheological models. Linear elastic and viscoelastic models of tissues have a long history (for example see Fung (1981)) and more recent examples of comparisons of different models in the context of elastography data include Klatt *et al* (2007) and Carstensen and Parker (2014).

The microchannel flow model (MFM) was introduced to account for the behavior of soft, isotropic, vascularized tissue as an explicit result of fluid outflow under applied stress (Parker 2014a). A distribution of vessels and channels leads to a distribution of relaxation time constants by incorporation of Poiseuille's law, providing an overall relaxation spectrum characterized by a power law parameter. This single parameter characterizes the frequency dependence of the complex modulus, or stiffness of tissue as a function of frequency. The incorporation of upper and lower bounds on the distribution of time constants and vessel sizes, resulted in a 'four parameter' version of the microchannel flow model. We also derived the mapping function from the fractal branching vasculature to the relaxation spectrum of the material under uniaxial loading (Parker 2015b) and experimental results from altered samples were compared with theoretical predictions. The resulting tissue response changes in both stress relaxation measurements (time domain) and shear wave dispersion (frequency domain) were predicted from the microchannel flow model.

In this paper, we derive the frequency domain Fourier transform of the 4 parameter microchannel flow model and present predictions about the behavior of the complex modulus over frequency ranges relevant to magnetic resonance and ultrasound elastography. Finally, tissue measurements of liver and perfused placenta are compared against the microchannel flow model, providing strong evidence that the model can be useful for some mammalian tissues. The advantage of this approach is the strong tie of the MFM to anatomical and physiological states of the tissue including the fractal branching behavior of the vasculature and the upper and lower bounds on the sizes and time constants that result from the fluid channels and microchannels.

2. Theory

The microchannel flow model (Parker 2014a) begins by considering a block of liver tissue, comprised of a fine-scale interlocking structure of hepatic cells, connective tissue, and a multiplicity of fluid channels arising from its internal biliary, circulatory, and lymphatic systems, as shown in figure 1. The stress-strain relation for an idealized block of material with a single vessel and fluid outflow under uniaxial compression was considered.

Combining elastic and fluid outflow strains as additive is analogous to a Maxwell model of a series spring and dashpot; therefore the stress relaxation curve for a single vessel in an elastic substrate is a simple exponential decay function. Next, it is assumed that there are multiple microchannels of unequal radius r_n and therefore unequal time constants τ_n where Poiseuille's Law provides the r^{-4} proportionality between r_n and τ_n . If each contributes to the stress relaxation at their respective time constant τ_n , then the simplest model is a parallel set of Maxwell elements. The generalized Maxwell-Wiechert model (Ferry 1970, Fung 1981) incorporates these multiple parallel elements in conjunction with an optional single spring element. The stress relaxation solution for N Maxwell elements can be written as a Prony series (Lakes 1999)

$$\sigma_{\text{SR}}(t) = \sum_N A_N e^{-t/\tau_N} \quad (1)$$

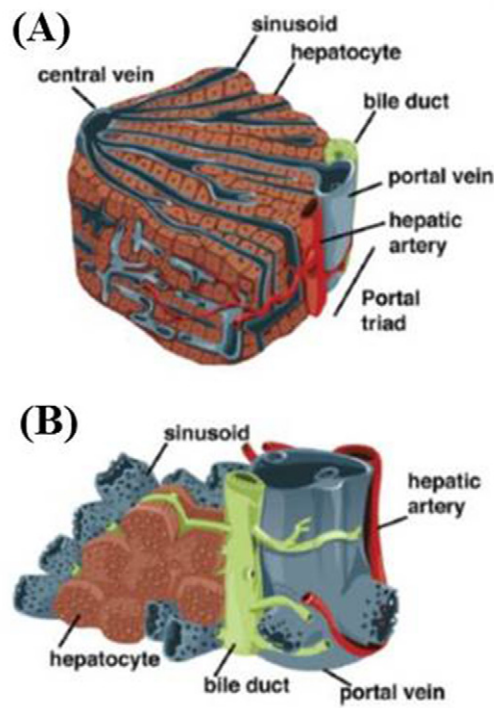


Figure 1. (A) Illustration showing overall structure of a portion of a liver lobule. (B) Higher resolution of the relationship between key cellular compartments of the liver (Reprinted from Si-Tayeb *et al* 2010, with permission from Elsevier).

where A_N are the relative strengths of the components with characteristic relaxation time constant τ_N . In the limit of continuous distribution of time constants τ , the summation becomes an integral and $A(\tau)$ is the relaxation spectrum, which can be either discrete or continuous, depending on the particular medium under study (Fung 1981). Given a material's $A(\tau)$, we can write:

$$\sigma_{\text{SR}}(t) = \int_0^{\infty} A(\tau) e^{-t/\tau} d\tau \quad (2)$$

Now consider a specific power law distribution:

$$A(\tau) = A_0 \tau^{-b}; 1 < b < 2 \quad (3)$$

The power law distribution is naturally occurring in many natural structures including normal and pathological circulatory systems (Risser *et al* 2007). Substituting equation (3) into equation (2) and solving yields the solution:

$$\sigma_{\text{SR}}(t) = A_0 \cdot t^{1-b} \Gamma [b - 1] \text{ for } 1 < b < 2, t > 0 \quad (4)$$

where Γ is the Gamma function. The stress relaxation response is characterized by $1/t^{b-1}$ decay for $t > 0$.

The Fourier transform of the derivative (impulse response) of equation (4) gives the frequency dependence of the complex modulus:

$$E(\omega) = \frac{A_0}{\sqrt{2\pi}} \Gamma[a] \Gamma[1-a] \text{Abs}[\omega]^a \left(\cos\left[\frac{a\pi}{2}\right] + i \cdot \text{Sign}[\omega] \sin\left[\frac{a\pi}{2}\right] \right) \tag{5}$$

where $i = \sqrt{-1}$. This response is dominated by the steady increase with frequency to the power of $a = b - 1$, for $b > 1$ and $a > 0$.

In practical cases it might be realistic to place limits on the range of τ for a material, reflecting the longest and shortest time constraints that pertain to the smallest to largest vessels and microchannels. In this case, the integration of equation (2) has limits τ_{\min} and τ_{\max} and

$$\sigma_{\text{SR}}(t) = \int_{\tau_{\min}}^{\tau_{\max}} A(\tau) e^{-t/\tau} d\tau \tag{6}$$

Assuming the power law form of equation (3), then

$$\sigma_{\text{SR}}(t) = A_0 \left(\frac{\Gamma\left[a, \frac{t}{\tau_{\max}}\right] - \Gamma\left[a, \frac{t}{\tau_{\min}}\right]}{t^a} \right) \text{ for } a > 0, t \geq 0, \text{ and } 0 < \tau_{\min} < \tau_{\max}, \tag{7}$$

where $\Gamma\left[a, \frac{t}{\tau}\right]$ is the incomplete Gamma function (upper-tailed). This version of the micro-channel flow model is a four parameter model since τ_{\max} and τ_{\min} must be determined as material-specific parameters in addition to a and A_0 .

The physical meaning of these parameters are as follows: A_0 is set by the basic elastic modulus E of the solid material comprising the structure; the power law a (or $b = a + 1$) is related to the fractal branching vasculature; τ_{\max} and τ_{\min} are time constants of flow related by Poiseuille’s Law to the smallest and largest vessels, respectively, within a representative sample volume of the vascularized material.

A more general solution to equation (6), valid for the power law parameter $b > 0$ is:

$$\sigma_{\text{SR}}(t) = A_0 \left\{ \tau_{\max}^{(1-b)} \text{EIE}\left(2-b, \frac{t}{\tau_{\max}}\right) - \tau_{\min}^{(1-b)} \text{EIE}\left(2-b, \frac{t}{\tau_{\min}}\right) \right\} \text{ for } t \geq 0, \tag{8}$$

where $\text{EIE}(n, z)$ is the exponential integral function $E_n(z)$ (Abramowitz and Stegun 1964). The Fourier transform of this according to Mathematica (Wolfram Research, Champaign, IL, USA) is:

$$\frac{A_0}{\sqrt{2\pi}} \left[\begin{aligned} & \left. \left. \begin{aligned} & \tau_{\min}^{(2-b)} \left(\frac{i \cdot \tau_{\min} \cdot \omega \cdot H2F1\left[1, \frac{3-b}{2}, \frac{5-b}{2}, -\tau_{\min}^2 \omega^2\right]}{-3+b} + \frac{H2F1\left[1, 1-\frac{b}{2}, 2-\frac{b}{2}, -\tau_{\min}^2 \omega^2\right]}{-2+b} \right) \right. \\ & \left. \tau_{\max}^{(2-b)} \left(\frac{-i \cdot \tau_{\max} \cdot \omega \cdot H2F1\left[1, \frac{3-b}{2}, \frac{5-b}{2}, -\tau_{\max}^2 \omega^2\right]}{-3+b} + \frac{H2F1\left[1, 1-\frac{b}{2}, 2-\frac{b}{2}, -\tau_{\max}^2 \omega^2\right]}{2-b} \right) \right] \end{aligned} \right. \tag{9}$$

where $H2F1[a, b, c, z]$ is the hypergeometric function ${}_2F_1(a, b, c, z)$ (Abramowitz and Stegun 1964).

The complex modulus $E(\omega)$ for the material is given by the Fourier transform of the impulse response, which is related to the stress relaxation response by a time derivative, or $i \cdot \omega$ in the frequency domain. Accordingly, the magnitude of the complex modulus $|E(\omega)|$ is given by the magnitude of $i \cdot \omega \cdot$ equation (9). To illustrate the stress relaxation behavior (time domain) and complex modulus (frequency domain), equations (8) and (9) are plotted in

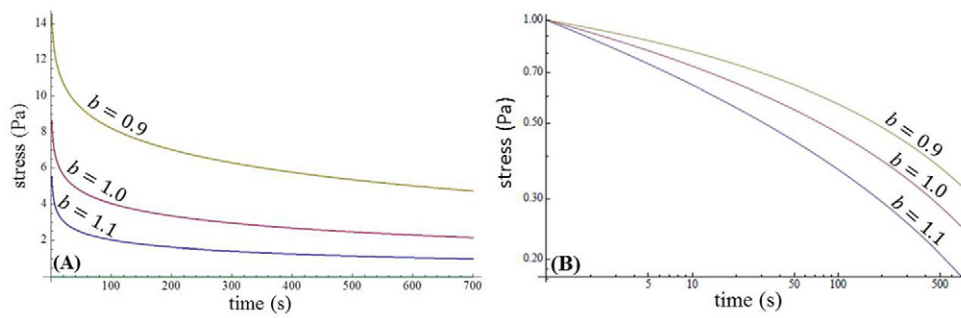


Figure 2. (A) Time domain stress relaxation curves using the 4 parameter model with only the power law variable, b , changed. The drop in amplitude of the curves is due to the decreased area under the integration of equation (6). (B) Log–log plot of the same three cases as 2(A), however with the stress relaxation forces all normalized to unity at 1 s. This demonstrates the different decay rates corresponding to the power law parameter b of the stress relaxation spectrum.

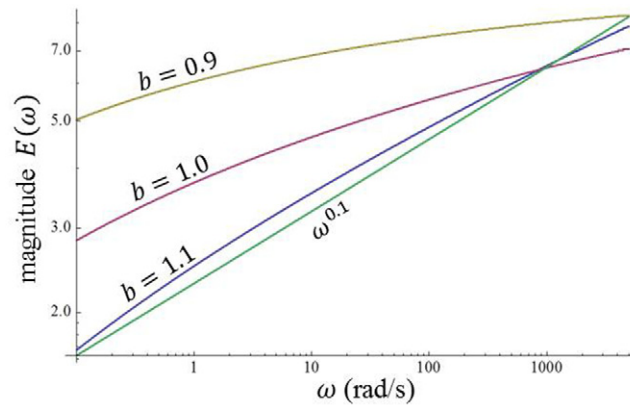


Figure 3. Log–log plot of complex modulus using the four parameter model but varying only the power law parameter of $b = 0.9, 1.0, 1.1$. In addition, a reference line of $\omega^{0.1}$ is shown for comparison.

figures 2 and 3 using the parameters $A_0 = 1$, $\tau_{\min} = 1/3000$ s, $\tau_{\max} = 10\,000$ s, and the power law parameter b is varied. The parameters are suggested by previous results in liver (Parker 2015b).

The frequency domain behavior of the complex modulus $|E(\omega)|$ corresponding to the same cases as figure 2 is given in figure 3. From top to bottom at 1 rad/s, the curves are: is $b = 0.9$, $b = 1.0$, and $b = 1.1$, respectively. In addition, the simple power law $\omega^{0.1}$ is set near the $b = 1.1$ case because in the 2 parameter version of the MFM, a power law parameter of $b = 1.1$ would result in a complex modulus frequency dependence of $a = (b - 1) = 0.1$. In all cases, the 4 parameter model does not obey a simple power law behavior because of the limits of integration over the relaxation spectrum.

These theoretical curves will be compared against results of tissue experiments in the next section.

3. Methods

3.1. Liver

Five whole veal (bovine) livers were obtained from a slaughterhouse and were transported on ice to our laboratories. Cylindrical liver samples (approximately 38 mm in diameter and 33 mm in length) were cut using a custom coring knife.

A QT/5 mechanical device (MTS Systems Co., Eden Prairie, MN, USA) with a 5 Newton load cell was used to test the core samples. The upper and lower plates were coated with vegetable oil before testing. The core samples were put on the center of the lower testing plate. The top plate was used as a compressor and carefully positioned to fully contact the sample. After two minutes for tissue recovery, uniaxial unconfined compression was applied to acquire the time domain stress relaxation data at room temperature under software control (TestWorks 3.10, Software Research Inc., San Francisco, CA, USA). The stress required to maintain compression was recorded for approximately 700s, and plotted as stress versus time under 10% strain.

The stress relaxation curve of each sample during the hold period was fitted to the micro-channel flow model (MATLAB, The MathWorks Inc., Natick, MA, USA). The trust-region method for nonlinear least squares regression was applied on each curve. Crawling wave (interfering shear wave) measurements in the liver were obtained using the methods reported in Zhang *et al* (2007) and Barry *et al* (2012, 2014). Shear wave measurements in the liver were also taken using a Siemens Antares scanner (Siemens Medical Solutions, Malvern, PA, USA) and VF10-5 probe (Siemens Medical Solutions, Malvern, PA, USA) at 5 MHz with our custom single-track-location shear wave elasticity imaging (STL-SWEI) pulse sequences and accelerated processing (McAleavey *et al* 2009).

3.2. Placenta

Nine human placentae from healthy and uncomplicated term pregnancies were obtained immediately after caesarean section. The study protocol was reviewed and approved by the Research Subjects Review Committee at the University of Rochester. Since the placenta is a surgical tissue specimen for disposal and no patient identifiers were associated with the tissue sample, patient consent was not required, in accord with the World Medical Association Declaration of Helsinki. The post-delivery placentae were examined for gross defects before catheters were introduced and secured in fetal veins and arteries with sutures, tissue cement, or both. The arterial catheters were connected to a pump (Miller *et al* 1985, 1993) and the placenta placed fetal side (chorionic plate) up in a 37 °C water bath. An open perfusion system (i.e. without recirculation) provided fetal flows at ~3–6 ml min⁻¹ while maintaining fetal arterial pressure <40 mm Hg under control conditions. The applied fetal pressures were not as pulsatile as in the *in vivo* systolic and diastolic maternal and fetal pressures but maintained a normal range of flow and pressure in the system. Multiple aspects of placental functions can be studied in this manner, including hemodynamics, transplacental transport, cellular uptake, endocrine function, and metabolism. Criteria for effective dual perfusion have been published previously (di Sant'Agnes *et al* 1987, Miller *et al* 1993); those most commonly employed are oxygen consumption, glucose consumption, lactate production, human chorionic gonadotropin production, net fetal oxygen transfer, fetal pressure, and flow rates.

Placental elastography images were generated using a Siemens Antares scanner (Siemens Medical Solutions, Malvern, PA, USA) and VF10-5 probe (Siemens Medical Solutions, Malvern, PA, USA) at 5 MHz with our custom STL-SWEI pulse sequences and accelerated processing (McAleavey *et al* 2009). Perfused placentae were placed on an acoustically-absorbing pad immersed in a 37 °C buffered saline bath, and scanned.

For STL-SWE dispersion calculations we used the methods described by Deffieux *et al* (2009) and extended by Parker and Baddour (2014) and Elegbe and McAleavey (2013). After a radiation force push pulse is applied to tissue, the velocity versus time data are collected at a minimum of two positions to assess the shear wave propagation. A Fourier transform of the tissue velocity field permits computation of phase and amplitude components as a function of frequency. Assuming the Green's function for propagation in cylindrical coordinates (Hankel functions) is valid, the phase velocity can be calculated as a function of frequency, typically between 100 Hz and 600 Hz in tissues.

The transducer was placed in a plastic sleeve containing room temperature ultrasound gel, supported by a mechanical arm and lowered into the bath without applying pressure to the fetal placental surface. The transducer was repositioned where an area of flow could be demonstrated in Doppler color mode. Since the perfusate did not contain red blood cells, the ultrasound contrast agent (UCA) Optison (GE Healthcare, Wauwatosa, WI, USA) was injected into the arterial side of the fetal circuit to enhance perfusate scattering and Doppler flow signals. Boluses of 0.1–0.5 c.c. were injected into the perfusate reservoir supplying the fetal circuit. Two vasoactive substances were also employed in five of the placenta experiments. First, U46619 (Caymen Chemical Co., Ann Arbor, MI, USA), a thromboxane agonist and a potent vasoconstrictor, was injected into the fetal artery. The dose (1 ml, 10^{-6} M) corresponded to amounts used previously by other authors (Maguire *et al* 1998, Myatt *et al* 1998, Abramowicz *et al* 1999). After 10 or more minutes, and prior to barium contrast injection, 1 ml of nitroglycerin (American Regent Inc., Shirley, NY, USA), a potent vasodilator, was injected. Finally, the whole post-delivery placenta was perfused with a 30% barium sulfate: 1% agarose suspension and then scanned at highest resolution in our clinical Philips Diamond Select Brilliance 64 channel CT scanner (Philips Healthcare, Andover, MA, USA) with 0.25 mm resolution in-plane and 0.6 mm in thickness.

To quantify the fractal dimension of the vasculature in the high resolution 3D computed tomography (CT) data, a Sholl analysis was performed on the barium-filled vasculature after segmentation (Milosevic and Ristanovic 2007). Similar to other multi-scale metrics, the analysis begins with an initial position and small radius, and counts the intersections of the vessels with the Sholl sphere. The radius is increased in small increments to cover an increasing range of scales. The log–log method (log of intersections versus log of radius) has been shown to correlate well with other measures of fractal dimension (Caserta *et al* 1995).

4. Results

4.1. Liver

Liver dispersion values from one liver (representative of the five studied) are shown in figure 4. A lower frequency range was probed by crawling waves over a relatively large (4 cm \times 4 cm) ROI; higher frequencies were probed by the STL-SWEI where approximately 2 mm separations between measurement points are common, and the measurements are then taken repeatedly over a larger ROI. In spite of the difference in protocol, the results were quite consistent, matching the 2 parameter MFM theoretical curve (equations (4) and (5)) derived from independent mechanical stress relaxation measurements of 6 cores from the same liver lobes, with $b = 1.2$. Thus, liver dispersion approximates the power law behavior of equation (5), as reported previously (Zhang *et al* 2007).

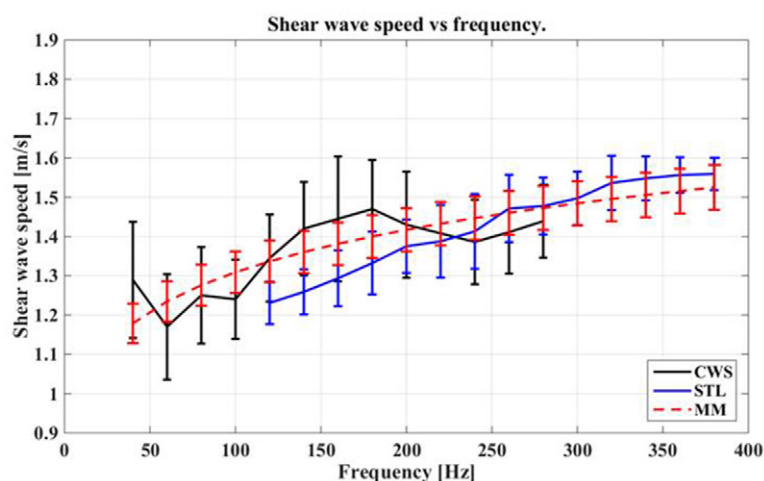


Figure 4. Shear wave speed versus frequency, demonstrating agreement between three different measurements: crawling waves, STL-SWEI, and a theoretical 2 parameter MFM with parameters derived from independent mechanical stress relaxation measurements on 6 core samples from the same liver.

4.2. Placenta

STL-SWE images from the normal perfused placentae generally demonstrated shear wave speeds in the range of 1.5 to 2.5 m s^{-1} with some local variations. Figure 5 shows the results from a ROI in one placenta where the stiffness had a marked increase shortly after administration of the U46619 vasoconstrictor agent.

The effects of the vasoconstrictor were generally seen to have regional variations, and were not uniform across the region of interest. This regional or ‘focal’ distribution of response has been noted previously (Whittle *et al* 1985, Abramowicz *et al* 1999). Thus, the results of figure 5 are representative, but the measured values in any experiment will depend on the size and location of the shear wave speed ROI with respect to the regional variations in vasoconstriction. Further examples are given in (McAleavey *et al* 2016).

The MFM explicitly states that the measured elastic response of the tissue will depend on the fractal branching vasculature (which sets the power law parameter b) and the size distribution of the vasculature (which sets the $A(\tau)$ and the limits of integration of equation (6)). Thus, the architecture of the placenta vasculature is germane to the applicability of the model. Figure 6 demonstrates a high resolution CT image of barium contrast-enhanced placental vasculature. After skeletonization, a multi-scale analysis of the branching vascular tree was performed, in particular a log–log Sholl analysis which is computationally efficient and is related to the fractal dimension (Caserta *et al* 1995). In this case, a slope of nearly 2 is found within a region of measurement scales falling within the placenta. This slope is close to values of fractal dimension found from other analyses of vascular beds (Risser *et al* 2007).

The 4 parameter MFM was then used to approximate the placenta results, guided by tissue parameters reported previously for liver and using the relation that the phase velocity is proportional to the square root of the magnitude of the complex modulus (Zhang *et al* 2007, Parker 2014a). Figure 5(B) includes the theoretical predictions for the case of the top curve ($A, \tau_{\min}, \tau_{\max}, b$) = (0.54 kPa, $(1/6) \times 10^{-3}$ s, 72×10^3 s, 1.52) post-vasoconstrictor, and (0.54, $(1/6) \times 10^{-3}$, 9×10^3 , 1.42) for the bottom curve, before vasoconstriction. These values are not derived from a curve-fit optimum and are not unique. Rather, they are set by reference to

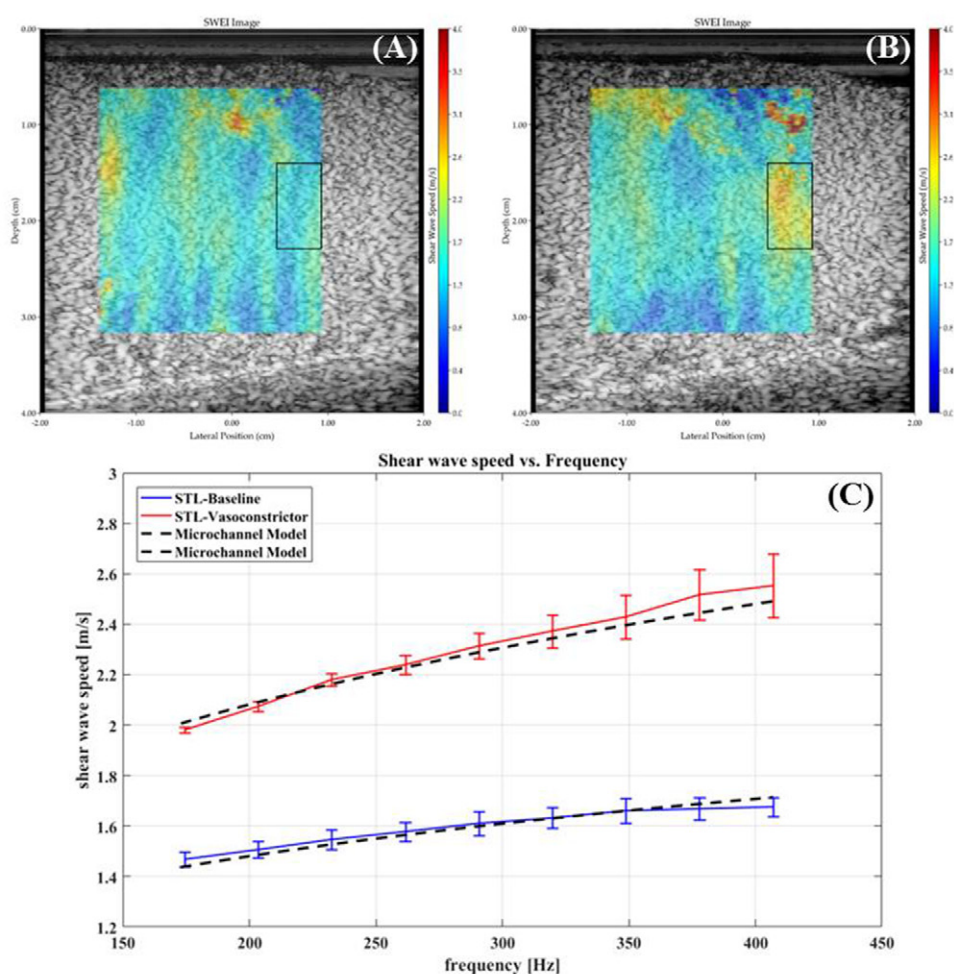


Figure 5. (A) Shear wave speed estimates overlaid as a color scale on a B-scan of perfused, post-delivery placenta. Region of interest box demarcates the area used for dispersion estimates. (B) The same region of interest post-vasoconstrictor shows a localized response producing elevated shear wave speeds. (C) Dispersion curves (shear wave speed versus frequency) for one *in vitro* perfused placenta. Administration of a potent vasoconstrictor agent results in a reduction of vasculature diameters and a corresponding increase in shear wave speed (upper curve). Theoretical shear wave speed dispersion curves guided by previous values and the expected influence of the vasoconstrictor on the vascular tree. Bottom curve, baseline measurement on perfused placenta, $b = 1.4$. Top curve, after vasoconstrictor, $b = 1.5$.

the MFM and stress relaxation results as follows: The A_0 are held identical at 0.54 to suppose no material change in the parenchyma during vasoconstriction. τ_{\min} is guided by previous results (Parker 2015b). The power law parameter b and τ_{\max} are allowed to change since vasoconstriction can produce a major shift in vessel diameters. Thus, these parameters are consistent also with the plausible behavior of the branching vascular tree, constricting across many branching generations some amount and also having some focal regions go into flow stasis (nearly complete blocking of flow in selected channels) (Whittle *et al* 1985).

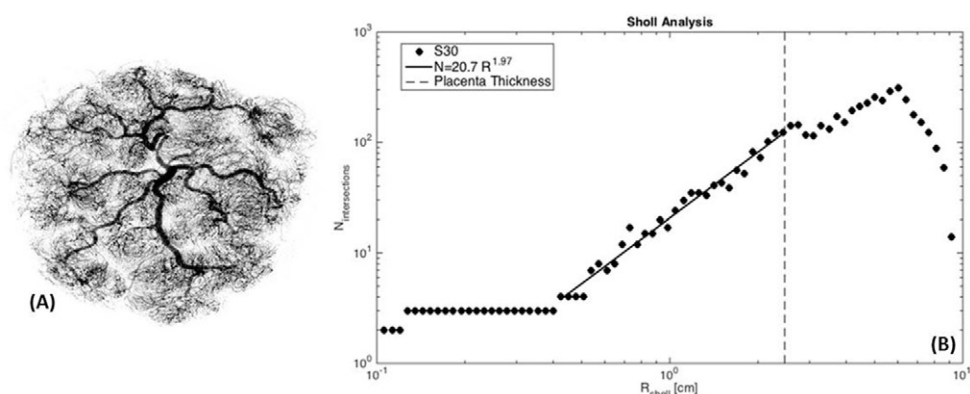


Figure 6. The fractal vascular tree of the post-delivery placenta. In (A) is the CT of the barium-enhanced vasculature. In (B) is the log–log Sholl analysis which is a multi-scale accounting of branches that is ultimately related to the fractal dimension.

5. Discussion

Different classes of biomechanical models have been applied successfully to a variety of tissues, including traditional spring and dashpot models (Fung 1981), the power law and fractional derivative models (Caputo 1967, Bagley and Torvik 1983, Suki *et al* 1994, Taylor *et al* 2001, Kiss *et al* 2004, Robert *et al* 2006, Zhang *et al* 2007, Holm *et al* 2013, Holm and Nasholm 2014), poroelastic models (Biot 1941, 1962, Mow *et al* 1980, 1984, Mak 1986, Miller and Chinzei 1997, Ehlers and Markert 2001, Konofagou *et al* 2001, Righetti *et al* 2004, Berry *et al* 2006, Cheng and Bilston 2007, Righetti *et al* 2007, Swartz and Fleury 2007, Perrinez *et al* 2009, 2010), linear hysteretic models (Carstensen and Parker 2014, Parker 2014b, 2015a), polymeric models (Ferry 1970) and compartmental models (Carstensen and Parker 2014).

An important question pertains to the link between the 4 parameter MFM considered in this study and the pre-existing models. There are a few obvious connections, first to spring-dashpot models. The derivation of the MFM works through the elastic material and fluid channels to arrive at the generalized Maxwell–Wiechert model, which in the continuous limit reduces to an integral equation across a power law relaxation function. So the link to spring-dashpot models explicitly exists via this pathway. Furthermore, the simplest two parameter version of the MFM is consistent with the Kelvin–Voigt Fractional Derivative (KVFD) model with E_0 set to zero (Zhang *et al* 2007, Parker 2014a), and this provides a connection to the general set of Power Law Attenuation models (Holm and Nasholm 2014). A third connection comes when the MFM parameter b is set to just slightly over unity, $b = 1 + \epsilon$. In this special case the material behavior, especially the dispersion and attenuation relations, approximate the ideal linear hysteresis model (Parker 2015a). Poroelastic models also consider the flow of fluid within a porous elastic medium however the governing assumptions are different (Darcy’s Law versus Poiseuille’s Law) and a detailed comparison is left for future work.

The microchannel flow model predicts a number of ways in which a sample of normal soft tissue such as liver can be modified so as to be perceived as less compliant, or hardened. First, any increase in the underlying elastic response characterized by E in the parallel Maxwell elements would increase the overall amplitude of the stress relaxation response. An increase in E might result from increasing the amount of collagen or fibrosis in tissue over time, or as a result of cross-linking (or ‘fixing’) specimens *ex vivo*. A second way to harden

a sample is less obvious because it involves the fluid flow. As the viscosity of the fluids in the microchannels increases, the resulting stress relaxation forces will increase according to the derivation of appendix 1 of Parker (2015b). This could apply to experiments where the hematocrit or temperature is changed (within limits of avoiding chemical or phase changes), or where the fluid is replaced by blood substitutes. Third, and less obvious, is the hardening caused by constriction of the smallest microchannels. This has a double effect in modifying the relaxation spectrum, and shifting it to the right (longer time constants) according to the derivation of appendix 2 of Parker (2015b). The net result is a modification that makes the specimen harder over prolonged intervals. This was experimentally approximated by inducing liver swelling from hypotonic saline in previous work (Parker 2015b). However *in vivo* this could be the net effect of inflammatory responses or edema. Finally, any modification of the fractal branching of the vasculature and fluid channels would affect the power law parameter b which drives dispersion. Possibly the action of vasoconstrictors or microemboli could make a rapid change in these parameters and therefore the effective tissue stiffness and shear wave dispersion.

Specifically, under the MFM the relation between the vasculature fractal dimension (power law parameter governing the number of vessels at each characteristic radius) f and the master power law parameter b was shown (Parker 2015b) to be: $b = (5 - f)/4$ where the integers are a result of the mapping from radius to time constants involving Poiseuille's Law and its r^{-4} dependence. In the case of our results, any b parameter above 1.25 would imply either the presence of an additional viscoelastic mechanism not included in the MFM, or else a case where f is negative, meaning that there are (pathologically) fewer small vessels than would be expected in normal tissue, with grossly altered hemodynamics. This scenario may be approached after application of the U46619 vasoconstrictor, where the measured stiffness and b parameter increased from 1.4 to 1.5 in response to the agent. However, it must be kept in mind that the specific parameters are only approximate and have a substantial degree of ambiguity.

Some limitations of this study include our current inability to make accurate, independent, repeated, and dynamic estimates of the fractal branching parameter of the vasculature. Estimates can be made from pathology slides or from contrast-enhanced 3D image sets, as shown in figure 6; however these are *ex post facto* measures and have their own sources of error.

A practical limitation of the four channel model is the ambiguity of estimated parameters when only limited data is available. As a specific example, consider an ideal specimen described perfectly by the parameters: (1000, 0.2, 1/333, 71 000). It can be shown that the stress relaxation curve between 10 and 500s for another specimen defined by (1050, 0.2, 1/333, 50 000) is very similar to the first specimen, differing by less than 4% over the curves from 10 to 500s. Here the first parameter (overall magnitude A) and the last parameter (τ_{\max}) are seen to 'trade off', at least over some limited period of observation of the responses. A similar situation exists when one only has a small bandwidth of shear wave speed estimates. Given this ambiguity plus noise and other sources of error, our ability to precisely determine the four parameters can be limited.

To extend the range of data and increase confidence, one can use multiple methods to increase the duration times and/or frequency bands. For example, Liu and Bilston (2000) utilized three methods to extend the frequency range of measurements of liver. Also, Zhang *et al* (2007) made use of the stress relaxation transient ramp plus the stress relaxation curves, adding emphasis to the most rapid time constants that are present in the early stages of the stress relaxation curve.

For *in vivo* studies, the emphasis is on shear wave speed estimates over some frequency range. In the results described herein, and in Ormachea *et al* (2013) and Ormachea (2015) the bandwidth of shear waves were extended by applying crawling wave techniques (applicable from 40–200 Hz) and then shear wave measurements from radiation force impulses (bandwidth 200–500 Hz). Furthermore, *a priori* or independent knowledge about the vasculature (see figure 6) can be used to set initial values or bounds on the parameters ($A, \tau_{\min}, \tau_{\max}$).

6. Conclusion

The microchannel flow model, and particularly the 4 parameter version, has attractive features because it captures both the time domain (stress relaxation) and frequency domain (shear wave dispersion) behavior of soft tissues over a biologically relevant range of durations and bandwidths. The model integrates parameters directly linked to tissue vascularity and fluid channels, so that altered conditions can be explicitly modeled and predicted.

Acknowledgments

The authors are grateful to Jonathan Langdon for implementation of the STL-SWEI, to Drs. Lorelei Thornburg and Tulin Ozcan for their advice and guidance on the placenta model. This work was supported by the University of Rochester School of Medicine and Dentistry and the University of Rochester Hajim School of Engineering and Applied Sciences.

References

- Abramowicz J S, Phillips D B, Jessee L N, Levene H, Parker K J and Miller R K 1999 Sonographic investigation of flow patterns in the perfused human placenta and their modulation by vasoactive agents with enhanced visualization by the ultrasound contrast agent Albutex *J. Clin. Ultrasound* **27** 513–22
- Abramowitz M and Stegun I A 1964 *Handbook of Mathematical Functions with Formulas, Graphs, and Mathematical Tables* (Washington, DC: US Government Printing Office)
- Bagley R L and Torvik P J 1983 A theoretical basis for the application of fractional calculus to viscoelasticity *J. Rheol.* **27** 201–10
- Berry G P, Bamber J C, Armstrong C G, Miller N R and Barbone P E 2006 Towards an acoustic model-based poroelastic imaging method: I. Theoretical foundation *Ultrasound Med. Biol.* **32** 547–67
- Barry C T, Hah Z, Partin A, Mooney R A, Chuang K-H, Augustine A, Almudevar A, Cao W, Rubens D J and Parker K J 2014 Mouse liver dispersion for the diagnosis of early-stage fatty liver disease: a 70-sample study *Ultrasound Med. Biol.* **40** 704–13
- Barry C T, Mills B, Hah Z, Mooney R A, Ryan C K, Rubens D J and Parker K J 2012 Shear wave dispersion measures liver steatosis *Ultrasound Med. Biol.* **38** 175–82
- Biot M A 1941 General theory of three-dimensional consolidation *J. Appl. Phys.* **12** 155–64
- Biot M A 1962 Mechanics of deformation and acoustic propagation in porous media *J. Appl. Phys.* **33** 1482–98
- Caputo M 1967 Linear models of dissipation whose q is almost frequency dependent-II *Geophys. J. R. Astron. Soc.* **13** 529–39
- Carstensen E L and Parker K J 2014 Physical models of tissue in shear fields *Ultrasound Med. Biol.* **40** 655–74
- Caserta F, Eldred W D, Fernandez E, Hausman R E, Stanford L R, Buldarev S V, Schwarzer S and Stanley H E 1995 Determination of fractal dimension of physiologically characterized neurons in two and three dimensions *J. Neurosci. Methods* **56** 133–44
- Cheng S and Bilston L E 2007 Unconfined compression of white matter *J. Biomech.* **40** 117–24

- Deffieux T, Montaldo G, Tanter M and Fink M 2009 Shear wave spectroscopy for *in vivo* quantification of human soft tissues visco-elasticity *IEEE Trans. Med. Imaging* **28** 313–22
- di Sant' Agnese P A, DeMeseey Jensen K, Miller R K, Wier P J and Maulik D 1987 Long term human placental lobule perfusion, an ultrastructural study *Trophoblast Res.* **2** 549–60
- Ehlers W and Markert B 2001 A linear viscoelastic biphasic model for soft tissues based on the theory of porous media *J. Biomech. Eng.* **123** 418–24
- Elegbe E C and McAleavey S A 2013 Single tracking location methods suppress speckle noise in shear wave velocity estimation *Ultrason. Imaging* **35** 109–25
- Ferry J D 1970 *Viscoelastic Properties of Polymers* (New York: Wiley)
- Fung Y C 1981 *Biomechanics: Mechanical Properties of Living Tissues* (Berlin: Springer)
- Holm S and Nasholm S P 2014 Comparison of fractional wave equations for power law attenuation in ultrasound and elastography *Ultrasound Med. Biol.* **40** 695–703
- Holm S, Näsholm S P, Prieur F and Sinkus R 2013 Deriving fractional acoustic wave equations from mechanical and thermal constitutive equations *Comput. Math. Appl.* **66** 621–9
- Kiss M Z, Varghese T and Hall T J 2004 Viscoelastic characterization of *in vitro* canine tissue *Phys. Med. Biol.* **49** 4207–18
- Klatt D, Hamhaber U, Asbach P, Braun J and Sack I 2007 Noninvasive assessment of the rheological behavior of human organs using multifrequency MR elastography: a study of brain and liver viscoelasticity *Phys. Med. Biol.* **52** 7281–94
- Konofagou E E, Harrigan T P, Ophir J and Krouskop T A 2001 Poroelastography: imaging the poroelastic properties of tissues *Ultrasound Med. Biol.* **27** 1387–97
- Lakes R S 1999 *Viscoelastic Solids* (Boca Raton, FL: CRC) pp 111–37
- Liu Z and Bilston L 2000 On the viscoelastic character of liver tissue: experiments and modelling of the linear behaviour *Biorheology* **37** 191–201 (PMID: 11026939)
- Maguire M H, Howard R B, Hosokawa T and Poisner A M 1998 Effects of some autacoids and humoral agents on human fetoplacental vascular resistance: candidates for local regulation of fetoplacental blood flow *Trophoblast Res.* **3** 203–14
- Mak A F 1986 Unconfined compression of hydrated viscoelastic tissues: a biphasic poroviscoelastic analysis *Biorheology* **23** 371–83 (PMID: 3779062)
- McAleavey S, Menon M and Elegbe E 2009 Shear modulus imaging with spatially-modulated ultrasound radiation force *Ultrason. Imaging* **31** 217–34
- McAleavey S A, Parker K J, Ormachea J, Wood R W, Stodgell C J, Katzman P J, Pressman E K and Miller R K 2016 Shear wave elastography in the living, perfused, post-delivery placenta *Ultrasound Med. Biol.* **42** 1282–8
- Miller K and Chinzei K 1997 Constitutive modelling of brain tissue: experiment and theory *J. Biomech.* **30** 1115–21
- Miller R K, Wier P J, Maulik D and di Sant' Agnese P A 1985 Human placenta *in vitro*: characterization during 12h of dual perfusion *Contrib. Gynecol. Obstet.* **13** 77–84 (PMID: 3995986)
- Miller R K, Wier P J, Perez-D'AGregorio R, Eisenmann C, di Sant' Agnese P A, Shah Y and Neth J L 1993 Human dual placental perfusions: criteria for toxicity evaluations *Methods Toxicol.* **3B** 246–59
- Milosevic N T and Ristanovic D 2007 The Sholl analysis of neuronal cell images: semi-log or log–log method? *J. Theor. Biol.* **245** 130–40
- Mow V C, Holmes M H and Lai W M 1984 Fluid transport and mechanical properties of articular cartilage: a review *J. Biomech.* **17** 377–94
- Mow V C, Kuei S C, Lai W M and Armstrong C G 1980 Biphasic creep and stress relaxation of articular cartilage in compression? Theory and experiments *J. Biomech. Eng.* **102** 73–84
- Myatt L, Eis A L W, Kossenjans W, Brockman D E, Greer I A and Lyall F 1998 Autocoid synthesis and action in abnormal placental flows reviewed: causative versus compensatory roles *Placenta* **19** 315–28
- Ormachea J 2015 Evaluation of shear wave speed measurements using crawling waves sonoelastography and single tracking location acoustic radiation force impulse imaging *MS Thesis, Digital Signal and Image Processing* Pontificia Universidad Católica del Perú, Lima, Peru
- Ormachea J, Salo A, Lerner A, McAleavey S and Castaneda B 2013 Comparison between crawling wave sonoelastography and STL-ARFI in biomaterials *Proc. 12th Int. Tissue Elasticity Conf. (Lingfield, UK)*
- Parker K J 2014a A microchannel flow model for soft tissue elasticity *Phys. Med. Biol.* **59** 4443–57
- Parker K J 2014b Real and causal hysteresis elements *J. Acoust. Soc. Am.* **135** 3381–9

- Parker K J 2015a Could linear hysteresis contribute to shear wave losses in tissues? *Ultrasound Med. Biol.* **41** 1100–4
- Parker K J 2015b Experimental evaluations of the microchannel flow model *Phys. Med. Biol.* **60** 4227–42
- Parker K J and Baddour N 2014 The Gaussian shear wave in a dispersive medium *Ultrasound Med. Biol.* **40** 675–84
- Parker K J, Doyley M M and Rubens D J 2011 Imaging the elastic properties of tissue: the 20 year perspective *Phys. Med. Biol.* **56** R1–29
- Perrinez P R, Kennedy F E, Van Houten E E, Weaver J B and Paulsen K D 2009 Modeling of soft poroelastic tissue in time-harmonic MR elastography *IEEE Trans. Biomed. Eng.* **56** 598–608
- Perrinez P R, Kennedy F E, Van Houten E E, Weaver J B and Paulsen K D 2010 Magnetic resonance poroelastography: an algorithm for estimating the mechanical properties of fluid-saturated soft tissues *IEEE Trans. Med. Imaging* **29** 746–55
- Righetti R, Ophir J, Srinivasan S and Krouskop T A 2004 The feasibility of using elastography for imaging the Poisson's ratio in porous media *Ultrasound Med. Biol.* **30** 215–28
- Righetti R, Righetti M, Ophir J and Krouskop T A 2007 The feasibility of estimating and imaging the mechanical behavior of poroelastic materials using axial strain elastography *Phys. Med. Biol.* **52** 3241–59
- Risser L, Flouraboue F, Steyer A, Cloetens P, Le Duc G and Fonta C 2007 From homogeneous to fractal normal and tumorous microvascular networks in the brain *J. Cereb. Blood Flow Metab.* **27** 293–303
- Robert B, Sinkus R, Larrat B, Tanter M and Fink M 2006 A new rheological model based on fractional derivatives for biological tissues 2006 *IEEE Ultrasonics Symp.* pp 1033–6
- Si-Tayeb K, Lemaigre K P and Duncan S A 2010 Organogenesis and development of the liver *Developmental Cell* **18** 175–89
- Suki B, Barabasi A L and Lutchen K R 1994 Lung-tissue viscoelasticity: a mathematical framework and its molecular basis *J. Appl. Physiol.* **76** 2749–59
- Swartz M A and Fleury M E 2007 Interstitial flow and its effects in soft tissue *Annu. Rev. Biomed. Eng.* **9** 229–56
- Taylor L S, Richards M S and Moskowitz A J 2001 Viscoelastic effects in sonoelastography: impact on tumor detectability 2001 *IEEE Ultrasonics Symp.* vol 2 pp 1639–42
- Whittle B J, Oren-Wolman N and Guth P H 1985 Gastric vasoconstrictor actions of leukotriene C₄, PGF₂ alpha, and thromboxane mimetic U-46619 on rat submucosal microcirculation *in vivo* *Am. J. Physiol.* **248** G580–6
- Zhang M, Castaneda B, Wu Z, Nigwekar P, Joseph J V, Rubens D J and Parker K J 2007 Congruence of imaging estimators and mechanical measurements of viscoelastic properties of soft tissues *Ultrasound Med. Biol.* **33** 1617–31